

Article

Enhancing the Low-Temperature CO Oxidation over CuO-Based α -MnO₂ Nanowire Catalysts

Yan Cui [†], Huikang Song [†], Yiyu Shi [†], Pengxiang Ge, Mindong Chen ^{*ID} and Leilei Xu ^{*}

Collaborative Innovation Center of Atmospheric Environment and Equipment Technology, Jiangsu Key Laboratory of Atmospheric Environment Monitoring and Pollution Control, School of Environmental Science and Engineering, Nanjing University of Information Science & Technology, Nanjing 210044, China; cuiyan@nuist.edu.cn (Y.C.); nuistshk@163.com (H.S.); syee@163.com (Y.S.); gepx@nuist.edu.cn (P.G.)

* Correspondence: chenmd@nuist.edu.cn (M.C.); leileixu88@nuist.edu.cn (L.X.); Tel.: +86-25-5873-1089 (M.C.)

[†] These authors contributed equally to this work.

Abstract: A series of CuO-based catalysts supported on the α -MnO₂ nanowire were facilely synthesized and employed as the CO oxidation catalysts. The achieved catalysts were systematically characterized by XRD, SEM, EDS-mapping, XPS and H₂-TPR. The catalytic performances toward CO oxidation had been carefully evaluated over these CuO-based catalysts. The effects of different loading methods, calcination temperatures and CuO loading on the low temperature catalytic activity of the catalyst were investigated and compared with the traditional commercial MnO₂ catalyst with a block structure. It was found that the slenderness ratio of a CuO/ α -MnO₂ nanowire catalyst decreases with the increase in CuO loading capacity. The results showed that when CuO loading was 3 wt%, calcination temperature was 200 °C and the catalyst that was supported by the deposition precipitation method had the highest catalytic activity. Besides, the α -MnO₂ nanowire-supported catalysts with excellent redox properties displayed much better catalytic performances than the commercial MnO₂-supported catalyst. In conclusion, the CuO-based catalysts that are supported by α -MnO₂ nanowires are considered as a series of promising CO oxidation catalysts.

Keywords: CuO-based catalyst; α -MnO₂ nanowire; low-temperature catalytic activity; CO oxidation



Citation: Cui, Y.; Song, H.; Shi, Y.; Ge, P.; Chen, M.; Xu, L. Enhancing the Low-Temperature CO Oxidation over CuO-Based α -MnO₂ Nanowire Catalysts. *Nanomaterials* **2022**, *12*, 2083. <https://doi.org/10.3390/nano12122083>

Academic Editors: Jihoon Lee and Ming-Yu Li

Received: 31 May 2022

Accepted: 14 June 2022

Published: 16 June 2022

Publisher's Note: MDPI stays neutral with regard to jurisdictional claims in published maps and institutional affiliations.



Copyright: © 2022 by the authors. Licensee MDPI, Basel, Switzerland. This article is an open access article distributed under the terms and conditions of the Creative Commons Attribution (CC BY) license (<https://creativecommons.org/licenses/by/4.0/>).

1. Introduction

Carbon monoxide is generally considered to be a fuel, resulting from the incomplete combustion of fuel. The environmental pollution it causes has become a serious problem all over the world, which has a great impact on human health and living environment [1,2]. At present, CO degradation technologies mainly include adsorption, separation, biodegradation, combustion, plasma catalysis, photocatalysis, catalytic oxidation and so on [3]. Among them, catalytic oxidation has been widely used because of its advantages of high purification efficiency, low reaction temperature and low cost [4]. Therefore, the design and development of catalysts with advanced performance is the key to solve CO catalytic oxidation. It was found that noble metals (Au [5], Pt [6] and Rh [7]) as the active center supported on specific metal oxides (CeO₂ [8], MnO₂ [9], ZrO₂ [10] and Fe₂O₃ [11]) with excellent oxygen storage capacity usually have high activity for CO catalytic oxidation. However, due to the high price and scarce resources of precious metals, their large-scale application is greatly limited. In the past few decades, various transition metal oxides (Co₃O₄, CuO, Fe₂O₃ and MnO₂) have proved to show excellent catalytic activity in CO catalytic oxidation. Co₃O₄-based catalysts have been widely studied for their low temperature catalytic activity that is similar to that of noble metal catalysts. However, the rapid deactivation of Co₃O₄-based catalysts occurs under high humidity [12,13]. In contrast, CuO-based catalysts have poor low temperature activity but high humidity tolerance. Therefore, the preparation of CuO-based catalysts with excellent low temperature activity has always been a research focus and challenge in the field of CO catalytic oxidation [14].

In order to design and prepare highly efficient CuO-based catalysts, the effect of catalyst supports and preparation strategies have been extensively studied. Among many catalyst supports, MnO₂ has been widely studied because of its low cost, environmental friendliness and high activity [15]. It is well known that the physicochemical properties of MnO₂ with different morphologies are often different. The common one-dimensional structures of MnO₂ include block structure, nanorods, nanotube and nanowires. Among these morphologies, MnO₂ of a nanowire structure plays an important role because nanowire with a one-dimensional structure can be used as the basic assembly unit of two- or three-dimensional structural materials [16,17]. In addition, composites with novel structures and properties can be prepared easily. Compared with traditional MnO₂ with a bulk structure, nanostructured MnO₂ materials generally have better physicochemical properties, such as a higher specific surface area, lower density and adjustable chemical properties [18]. In addition, various studies have shown that MnO₂ materials with nanowire morphology usually have a high surface area and strong metal-support interactions. Compared with other morphologies of MnO₂ nanomaterials, MnO₂ nanowire usually has higher catalytic activity [19,20]. Therefore, nanowire is the main form of MnO₂ nanomaterials. MnO₂ nanowires generally have more surface oxygen adsorption, stronger reducibility, higher specific surface area and lower Mn-O bond strength than MnO₂ nanorods. Therefore, it has a better catalytic performance in the catalytic combustion of dimethyl ether and the catalytic oxidation of toluene. Saputra et al. [21] found that MnO₂ nanowire exhibited higher activity than MnO₂ nanorods and MnO₂ nanofibers in the co-degradation of phenol by reactive oxygen species and hydroxyl groups. In addition, compared with nanorod and nanotube MnO₂, MnO₂ nanowires as supports have stronger interactions with Ag and exhibit higher toluene oxidation activity. Among the MnO₂ nanomaterials (α -MnO₂, β -MnO₂), α -MnO₂ nanowire also showed the best catalytic activity for CO, even after Co₃O₄ nanoparticles were decorated. Liang et al. [22] synthesized four MnO₂ nanomaterials with different crystal types. They found that the order of activity of CO catalytic oxidation is $\alpha = \delta > \gamma > \beta$ -MnO₂ because the $[2 \times 2]$ and $[1 \times 1]$ tunnel structures of α -MnO₂ can occupy more space to obtain more CO adsorption sites. On the other hand, the strong catalytic performance of α -MnO₂ for CO oxidation is due to the prolonged length of the Mn-O bond that is caused by twisted [MnO₆], which may be conducive to the fracture of Mn-O bond, thus promoting CO oxidation. Therefore, α -MnO₂ reacts easily with CO, which further improves its catalytic performance.

In addition, various studies have been carried out to improve the CO catalytic oxidation activity of MnO₂ nanowires. In order to achieve this goal, effective strategies, including element-doped surface engineering and combination with other active substances have been extensively developed [23]. Metal loading and doping are two commonly used modification methods for preparing catalysts. Both can significantly improve the catalytic activity of MnO₂ nanowires [24,25]. The loading method can disperse the metal or metal oxide on the surface of the catalyst carrier highly uniformly, and the catalyst with higher activity can be obtained due to the formation of a strong metal-support interaction. The doping method is to replace the metal cations in the main metal oxides with different cations, which can greatly change the chemical bonding on the surface of the main metal oxides and improve their catalytic performance [26,27]. The active sites in the catalytic system may be oxygen atoms near the dopant or the dopant itself. Therefore, the activity of MnO₂ nanowires can be further improved by dispersing more active components on their surfaces. Gao et al. [28] found that hydrothermal doping of Cu significantly improved the CO oxidation activity and water resistance of α -MnO₂ nanowires. For γ -MnO₂, Zn-doped MnO₂ achieves a 90% CO conversion at 160 °C and shows the best CO oxidation activity in other elements that are doped with γ -MnO₂. Li et al. [29] synthesized α -MnO₂ with a porous surface structure by acid treatment. It has rich adsorption sites for O₂, thus enhancing the catalytic oxidation activity of MnO₂ to CO. In addition, combining Au, Ag and CuO with MnO₂ nanomaterials can effectively improve the efficiency of CO catalytic oxidation. Xu et al. [30]

also studied the effect of a Ag-supported catalyst on CO catalytic oxidation activity on α -MnO₂ nanowires, and the T_{90%} of Ag/ α -MnO₂ could reach below 100 °C.

In this study, α -MnO₂ material with a perfect nanowire structure was successfully prepared by a one-step hydrothermal method. The nanowires with excellent structural properties and thermal stability could be used as CuO-based catalyst supports. A series of CuO-based α -MnO₂ nanowire catalysts were prepared by initial impregnation and deposition precipitation methods for CO catalytic oxidation reaction at a low temperature. The catalysts were characterized by X-ray powder diffraction (XRD), scanning electron microscopy (SEM), energy-dispersed spectroscopy (EDS) mapping, X-ray photoelectron spectroscopy (XPS), etc. The effects of different loading methods, calcination temperature, CuO loading and the mesoscopic structure of MnO₂ on CO oxidation activity at low temperature were studied.

2. Materials and Methods

2.1. Synthesis of α -MnO₂ Nanowire Support

The α -MnO₂ nanowire support was synthesized by a hydrothermal method according to the scheme that was previously reported [31]. Specifically, 3 mmol of MnSO₄·H₂O was first dissolved in 40 mL of deionized water and stirred for 5 min until the MnSO₄·H₂O solution was clarified. Then, 2 mmol of KMnO₄ was also dissolved in 40 mL of deionized water and stirred for 5 min. After that, the KMnO₄ solution was gradually added to the MnSO₄·H₂O solution to obtain the brown suspension, and the stirring was continued for 30 min. The stirred brown suspension was transferred to a Teflon reactor and hydrothermal reaction at 160 °C for 12 h. The brown-black liquid that was obtained after the hydrothermal treatment was washed six times with ethanol. The solid that was obtained by centrifugation was placed in a vacuum drying oven at 100 °C for 12 h, and then the α -MnO₂ nanowire support was obtained.

2.2. CuO-Based α -MnO₂ Nanowire Catalyst Preparation

The CuO-based supported α -MnO₂ nanowire catalysts containing x wt% CuO ($x = m_{\text{CuO}} / (m_{\text{CuO}} + m_{\text{support}}) \times 100\%$) were synthesized by a deposition precipitation method. To be specific, α -MnO₂ nanowire was dispersed in Cu(NO₃)₂·3H₂O solution, and then Na₂CO₃ (0.01 M) solution was added droplet by droplet to adjust the pH to 8–9. The mixed solution was fully stirred for 30 min and then stood for 1 h. After filtration, it was washed with deionized water and dried for 12 h in an oven of 120 °C. Then, the CuO-based α -MnO₂ nanowire catalysts with different CuO loading were obtained by calcination at 200 °C for 5 h and were denoted as $x\text{CuO}/\alpha\text{-MnO}_2\text{-200-DP}$ ($x = 1, 3, 5, 10, 20$ and 30). Meanwhile, a series of catalysts defined as $3\text{CuO}/\alpha\text{-MnO}_2\text{-}T\text{-DP}$ ($T = 120, 200, 300$ and 400) were synthesized under the same preparation process at a different calcination temperature, where “ T ” refers to the calcination temperature of the catalyst. In order to clarify the influence of the loading mode on the performance of the catalyst, the CuO-based α -MnO₂ nanowire catalyst by incipient impregnation method was denoted as $3\text{CuO}/\alpha\text{-MnO}_2\text{-200-IMP}$.

In addition, the CuO that was supported on a commercial MnO₂ catalyst ($3\text{CuO}/\text{C-MnO}_2\text{-200-DP}$) indicated that the special morphology of α -MnO₂ nanowire also promoted the catalytic activity of CO catalytic oxidation. The commercial MnO₂ that was used in this study was the most common one in the market, and it was normal to have fewer impurities in the commercial MnO₂.

2.3. Catalyst Characterizations

X-ray powder diffraction (XRD) patterns of all catalysts were performed on a Smart Lab/3 kW Intelligent multifunctional X-ray Diffractometer (Shimadzu, Kyoto, Japan) (Cu K α radiation 40 kV/100 mA, the step of 5°/min, 2 θ = 10–80°). Scanning electron microscopy (SEM) and energy-dispersed spectroscopy (EDS) mapping measurements of all catalysts were carried out on a scanning electron microscopy (FEI TECNAI G2 F20, Hillsboro, OR, USA). The sample was glued to the conductive adhesive, and gold spraying was

performed for 45 s and 10 mA using Oxford Quorum SC7620 sputtering coater (Quorum, UK). The morphology of the sample was photographed with a ZEISS Gemini SEM 300 scanning electron microscope. The X-ray photoelectron spectroscopy (XPS) measurements were tested on an Escalab 250Xi (Thermo Fisher Scientific, Waltham, MA, USA) that was equipped with an Al K α X-ray source to determine the elemental composition and chemical states of the elements. The powder of the sample was spread and coated on conductive tape on the sample holder. The binding energies were calibrated using the C 1s line at 284.5 eV as the reference.

H₂ temperature-programmed reduction (H₂-TPR) experiments were carried out in a self-made fixed-bed reactor (assembly). The consumption curve of H₂ was recorded and analyzed by an online LC-D200 mass spectrometer (TILON, Seoul, Korea). A mixture of H₂ (0.4 mL/min) and Ar (7.6 mL/min) was introduced into the reactor. After the H₂ signal baseline ($m/z = 2$) was stabilized, a H₂-TPR experiment was performed at a heating rate of 20 °C/min from room temperature to 800 °C.

2.4. Catalyst Evaluation

The catalytic activity of CO oxidation of the catalyst in this system had been tested in a vertical fixed-bed continuous flow reactor that was equipped with quartz tubes (I.D. = 10.00 mm). The temperature of the reaction should be the center temperature of the catalyst bed and it was detected and controlled by the thermocouple that was located in the center of the catalyst bed. The gas flows of the feed gases are controlled by the mass flow controllers (MFC, Brooks Instrument, Hatfield, UK) and used as feed 1 vol % CO, 20 vol. % O₂ and balanced N₂. The catalyst weighed 0.1 g and was injected with CO reaction gas with a total flow of 20 mL/min. The CO oxidation corresponding to the gas hourly space velocity (GHSV) was 12,000 mL/(g·h) gas, and the catalytic activity of CO oxidation over different catalysts was tested in the specified temperature range. Finally, a GC-680 gas chromatograph (Perkin Elmer, Waltham, MA, USA) with a thermal conductivity detector (TCD) was used for an on-line analysis of the outlet gas. The catalytic activity of the catalyst was reflected and expressed by CO conversion. The conversion rate of CO was calculated based on the formula below:

$$C_{CO} = \frac{F_{CO,Inlet} - F_{CO,Outlet}}{F_{CO,Inlet}} \times 100\% \quad (1)$$

$F_{CO,Inlet}$ represented the flow rate of CO species into; $F_{CO,Outlet}$ represented the flow rate of CO species out of the reactor.

3. Results and Discussion

3.1. Characterizations of the Catalysts

3.1.1. XRD Analysis

In order to study the crystal phase structure of the supports and catalysts, a series of materials were analyzed by XRD. In Figure 1, the diffraction peaks of α -MnO₂ that were located at $2\theta = 12.78^\circ, 18.11^\circ, 25.71^\circ, 37.52^\circ, 41.97^\circ, 49.86^\circ, 56.37^\circ, 65.11^\circ$ and 69.71° could be ascribed to the α -MnO₂ phase (PDF#44-0141) [30]. Specific, obvious diffraction peaks correspond to the (1 1 0), (2 0 0), (2 2 0), (2 1 1), (3 0 1), (4 1 1), (6 0 0), (5 2 1), (0 0 2) and (5 4 1) crystal planes of the MnO₂ structure, respectively. Figure 1a shows the XRD patterns of 3CuO/ α -MnO₂-200-DP and 3CuO/ α -MnO₂-200-IMP under different loading methods. As can be seen from the figure, the MnO₂ diffraction peak intensity of the 3CuO/ α -MnO₂-200-DP catalyst that was prepared by the deposition precipitation method (DP) loaded with CuO was significantly stronger than 3CuO/ α -MnO₂-200-IMP that was prepared by the initial impregnation method (IMP). The catalytic activity test showed that the CO catalytic oxidation activity of 3CuO/ α -MnO₂-200-DP was significantly better than that of 3CuO/ α -MnO₂-200-IMP. The test also proved that the (2 2 0) and (6 0 0) crystal planes of α -MnO₂ may play a dominant role in CO catalytic oxidation. At the same time, compared with the 3CuO/ α -MnO₂-200-IMP, the characteristic peak of CuO in

the 3CuO/ α -MnO₂-200-DP catalyst was much lower. The results showed that the CuO dispersion on the surface of the 3CuO/ α -MnO₂-200-DP catalyst was significantly higher than that of 3CuO/ α -MnO₂-200-IMP.

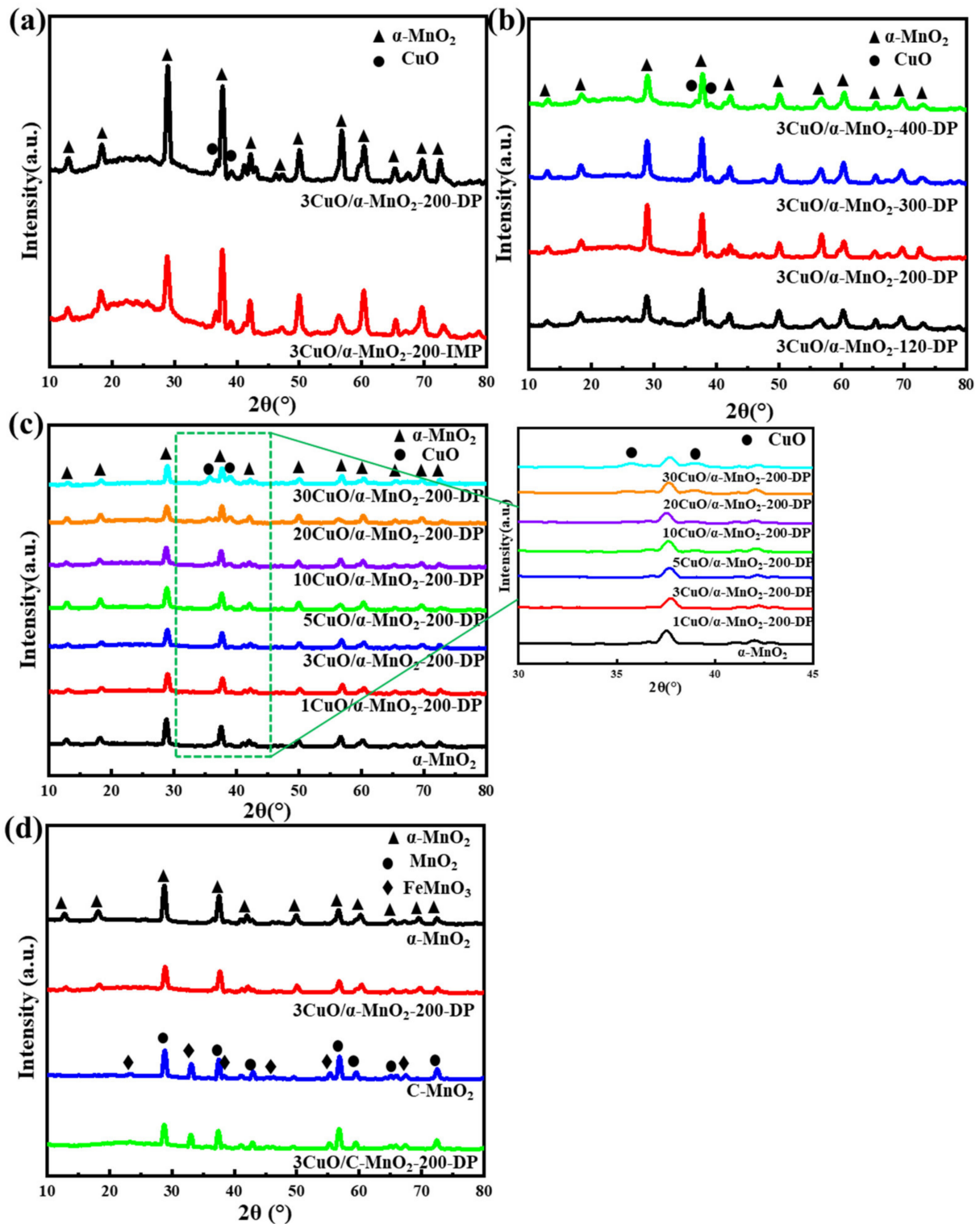


Figure 1. XRD patterns of (a) 3CuO/ α -MnO₂-200-DP and 3CuO/ α -MnO₂-200-IMP catalysts under different loading methods; (b) 3CuO/ α -MnO₂-*T*-DP (*T* = 120, 200, 300, 400) catalysts with different calcination temperatures; (c) *x*CuO/ α -MnO₂-200-DP (*x* = 0, 1, 3, 5, 10, 20, 30) catalysts with different CuO loading; (d) α -MnO₂ nanowire, commercial MnO₂ (C-MnO₂) and corresponding catalysts.

In general, calcination at higher temperatures was always accompanied by an increase in mean particle size and a decrease in specific surface area due to pore clogging. In addition to reducing the surface area, higher calcination temperatures reduced the active ingredients, ultimately leading to a reduction in the active interface sites. On the other hand, the CuO/ α -MnO₂ catalyst generated CuMn₂O₄ at higher temperature and deactivates [32]. Figure 1b shows the XRD patterns of 3CuO/ α -MnO₂-T-DP at different calcination temperatures. When the calcination temperature raised from 120 °C to 300 °C, the intensity of the XRD diffraction peak increased and the diffraction peak was the strongest at 300 °C. This ought to be attributed to the collapse of the nanowire framework at the calcination temperature as high as 300 °C, which made the dispersion of CuO worse. However, when the calcination temperature raised to 400 °C, the peak intensity decreased, which was caused by the formation of CuMn₂O₄. Moreover, due to the low content of CuMn₂O₄, its characteristic diffraction peak cannot be displayed in the XRD pattern.

The XRD patterns of the pure α -MnO₂ nanowire support and x CuO/ α -MnO₂-200-DP catalysts with different CuO loading are shown in Figure 1c. As can be seen from the figure, almost all the x CuO/ α -MnO₂-200-DP nanowire catalysts showed wide and clear XRD peaks, indicating that all the catalysts displayed good crystallinity. As the CuO loading increased, two diffraction peaks were detected at the $2\theta = 35.5^\circ$ and 38.8° , which were the diffraction peaks of CuO (PDF#05-0661) [33]. On the other hand, with the increase in CuO content, the intensity of the CuO diffraction peak also increased, indicating that the grain size of CuO increased. At the same time, the characteristic peak intensity of the (2 2 0) and (2 1 1) crystal planes of α -MnO₂ decreased obviously.

Figure 1d shows the XRD patterns of pure α -MnO₂ nanowire, commercial MnO₂ and corresponding catalysts. As can be seen from the figure, the diffraction peak of C-MnO₂ was the same as that of MnO₂ (PDF#72-1984). In addition, the diffraction peak of impurity FeMnO₃ (PDF#75-0894) was observed in the C-MnO₂ diffraction peak by comparison [34]. The characteristic peak of CuO cannot be clearly seen in the figure, due to the low loading of CuO. On the other hand, it indicated the high dispersion of CuO on the catalyst's surface.

3.1.2. SEM Observation

SEM images of the α -MnO₂ nanowire support and x CuO/ α -MnO₂-200-DP catalysts were analyzed, as shown in Figure 2. The 5CuO/ α -MnO₂-200-DP and 30CuO/ α -MnO₂-200-DP with different CuO loadings were selected as representative catalysts. Figure 2a,b shows the morphology of pure α -MnO₂ nanowire. It was found that the nanowire had a uniform morphology, smooth surface, and large aspect ratio (length: 5–15 μ m, width: 100–200 nm). Figure 2c,e, respectively, show the 5CuO/ α -MnO₂-200-DP and 30CuO/ α -MnO₂-200-DP nanowires' catalysts' structure. When the CuO loading increased from 0% to 5%, α -MnO₂ nanowire support retained its morphology, while the 30% CuO loading catalyst showed irregular nanowire. At the same time, the aspect ratio of α -MnO₂ nanowires decreases with the increase in CuO loading. The CuO loading was observed on the surface of the 5CuO/ α -MnO₂-200-DP and 30CuO/ α -MnO₂-200-DP catalysts.

The spatial dispersion of Mn and Cu elements in the nanowire structure could be characterized and analyzed by scanning transmission electron microscopy (STEM) and energy dispersive spectroscopy mapping (EDS-mapping) of the 3CuO/ α -MnO₂-200-DP and 3CuO/ α -MnO₂-200-IMP catalysts. It could be seen from Figure 3 that the supported metal Cu element was uniformly distributed on the surface of the catalysts. In addition, the dispersion of Cu element in the 3CuO/ α -MnO₂-200-DP catalyst was significantly higher than that of the 3CuO/ α -MnO₂-200-IMP catalyst, indicating that the catalyst that was prepared by the precipitation deposition method could better distribute the Cu element on the catalyst's surface.

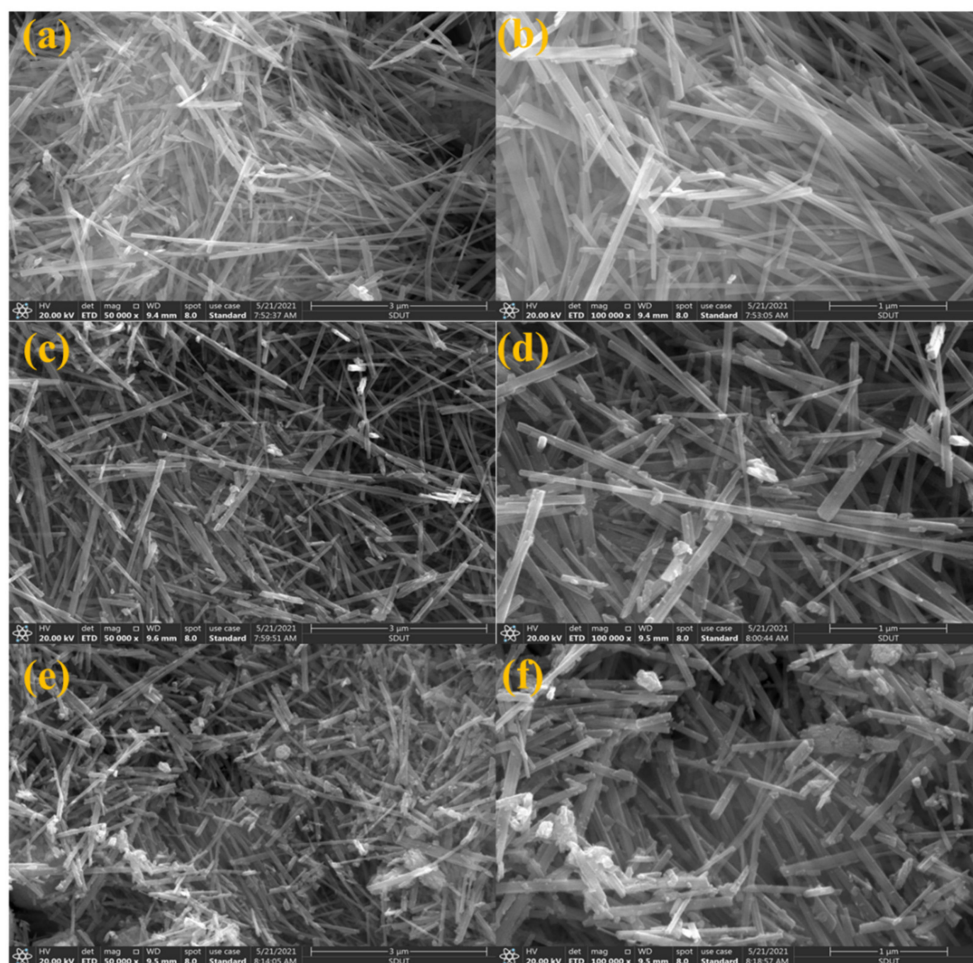


Figure 2. SEM images of α -MnO₂ nanowire support (a,b), 5CuO/ α -MnO₂-200-DP (c,d) and 30CuO/ α -MnO₂-200-DP (e,f) catalysts.

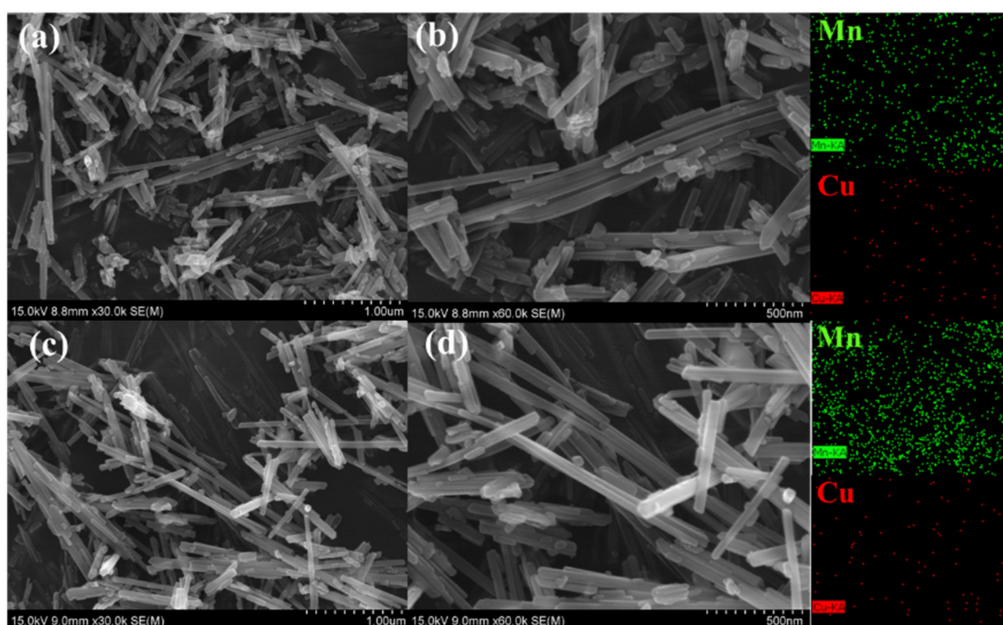


Figure 3. STEM and EDS element mapping images showing the spatial distribution of Mn and Cu elements: (a,b) 3CuO/ α -MnO₂-200-DP, (c,d) 3CuO/ α -MnO₂-200-IMP.

3.1.3. XPS Analysis

An XPS analysis of a series of prepared catalysts provided further evidence of surface chemical coordination, valence and composition states. Their XPS curves were shown in Figures 4–7. It can be seen from Figure 7 that the XPS spectrum of Mn 3s had a double peak structure, and the double peak spacing of all catalysts was 4.5 eV. Therefore, it could be concluded that the Mn species in all catalysts existed in the form of MnO₂. It can be seen from Figure 4a,c that the XPS distribution of Mn 2p and O 1s catalysts under different loading modes was almost the same, because the addition of a small amount of CuO did not affect the overall element concentration ratio of Mn and O. It can be observed from Figure 4b that these catalysts have two main peaks at 933.3 eV and 953.03 eV, which may be attributed to Cu 2p_{3/2} and Cu 2p_{1/2}, respectively. In addition, it was noteworthy that the Cu 2p_{3/2} peak was almost accompanied by an oscillating satellite peak in the range of 940.38–943.28 eV. This was accompanied by three satellite peaks with Cu 2p_{3/2} peaks at 940.4 eV (I), 941.8 eV (II), and 943.4 eV (III). It was well known that the satellite peak was caused by the transfer of electrons from the ligand orbit to the 3d orbit of Cu, which confirmed the existence of Cu²⁺ in the divalent form of the 3d⁹ structure, rather than the species level of Cu⁺ or Cu⁰ with d-filled energy [35,36]. Meanwhile, the XPS spectrum of Cu 2p varies greatly under different loading modes. The peak intensity of the Cu 2p spectrum of the 3CuO/α-MnO₂-200-IMP catalyst was significantly lower than that of the 3CuO/α-MnO₂-200-DP catalyst. The peak intensity of the Cu 2p spectrum of the 3CuO/α-MnO₂-200-IMP catalyst was significantly lower than that of the 3CuO/α-MnO₂-200-DP catalyst. The main reason for this was the different CuO dispersion over these catalysts. Specifically, the CuO dispersion of the 3CuO/α-MnO₂-200-IMP catalyst was poorer than the 3CuO/α-MnO₂-200-DP catalyst. According to the XPS survey spectra results (Table 1), the surface concentration of the Cu element over the 3CuO/α-MnO₂-200-DP catalyst was 2.9%, which was similar to the content of the Cu element that was added. However, the surface concentration (1.7%) of the Cu element in the 3CuO/α-MnO₂-200-IMP catalyst was much lower than the theoretical value. These results indicated that the deposition-precipitation method could better disperse the CuO than the initial impregnation method over the α-MnO₂ nanowire support.

The XPS spectra of Mn 2p, O 1s and Cu 2p at different calcination temperatures of the 3CuO/α-MnO₂-T-DP catalyst are shown in Figure 5. As can be seen from Figure 5a, these catalysts had two main peaks at 654.0 eV and 642.1 eV, which belong to Mn 2p_{1/2} and Mn 2p_{3/2} spin orbits, respectively. It should be noted that these two peaks were characteristic signals of Mn (IV). All these indicated the occurrence of interfacial reactions and the formation of MnO₂. To show the redox characteristics of the prepared catalyst, the surface oxidation state of copper was also studied [37]. As can be seen from Figure 5b, the XPS peaks that are centered on 954.0 eV and 933.0 eV belong to Cu 2p_{1/2} and Cu 2p_{3/2}, respectively. The binding energy of Cu 2p increased with the increase in calcination temperature. Meanwhile, with the increase in calcination temperature, the peak intensity corresponding to Cu 2p decreased, which may be caused by the decrease in Cu species' concentration on the catalyst surface, caused by the increase in calcination temperature. To further investigate the properties of various oxygen substances on the 3CuO/α-MnO₂-T-DP catalyst, the XPS spectrum of O 1s of 3CuO/α-MnO₂-T-DP are shown in Figure 5c. All the catalysts show two peaks of different oxygen species. Specifically, the peaks of 529.9 eV and 531.2 eV can be attributed to the lattice oxygen (O_{latt}) and surface-adsorbed oxygen (O_{ads}) of CuO_x and α-MnO₂, respectively. Combined with the data after peak fitting in Table 2, with the increase in calcination temperature, the atomic area ratio also decreased correspondingly. The oxygen vacancy concentration of 3CuO/α-MnO₂-200-DP was the highest. According to previous reports [38], the formation of oxygen anion radicals was due to the increased adsorption of environmental oxygen by surface oxygen vacancies, which will further improve the performance of catalysts.

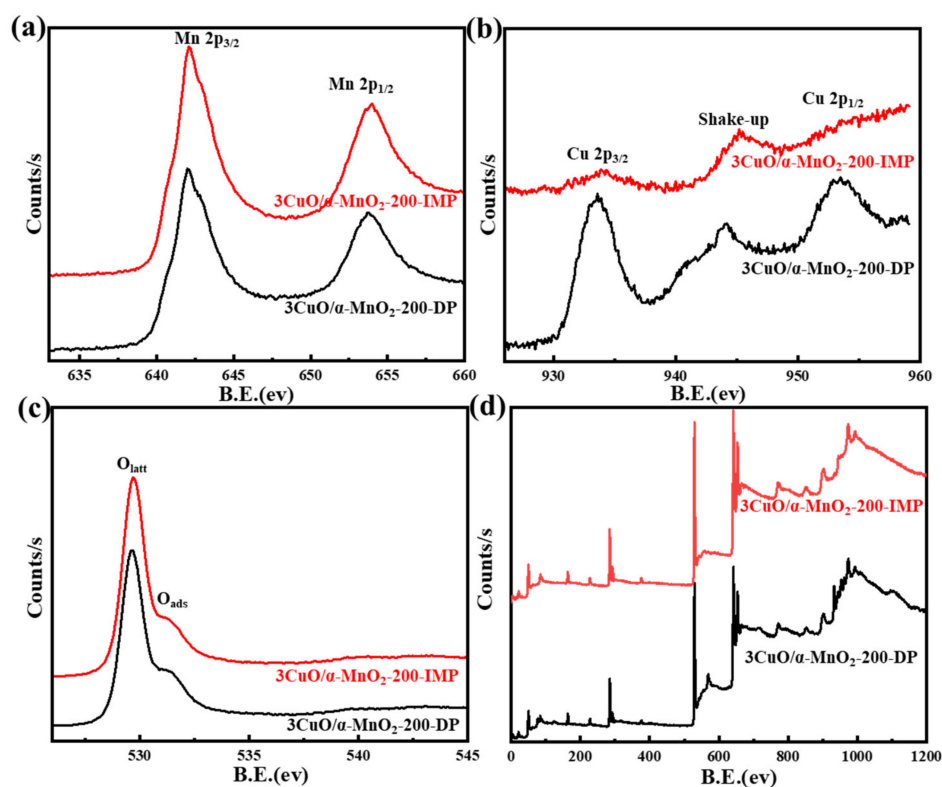


Figure 4. XPS spectra of Mn 2p (a), Cu 2p (b), O 1s (c) and survey spectrum (d) for 3CuO/α-MnO₂-200-DP and 3CuO/α-MnO₂-200-IMP catalysts under different loading methods.

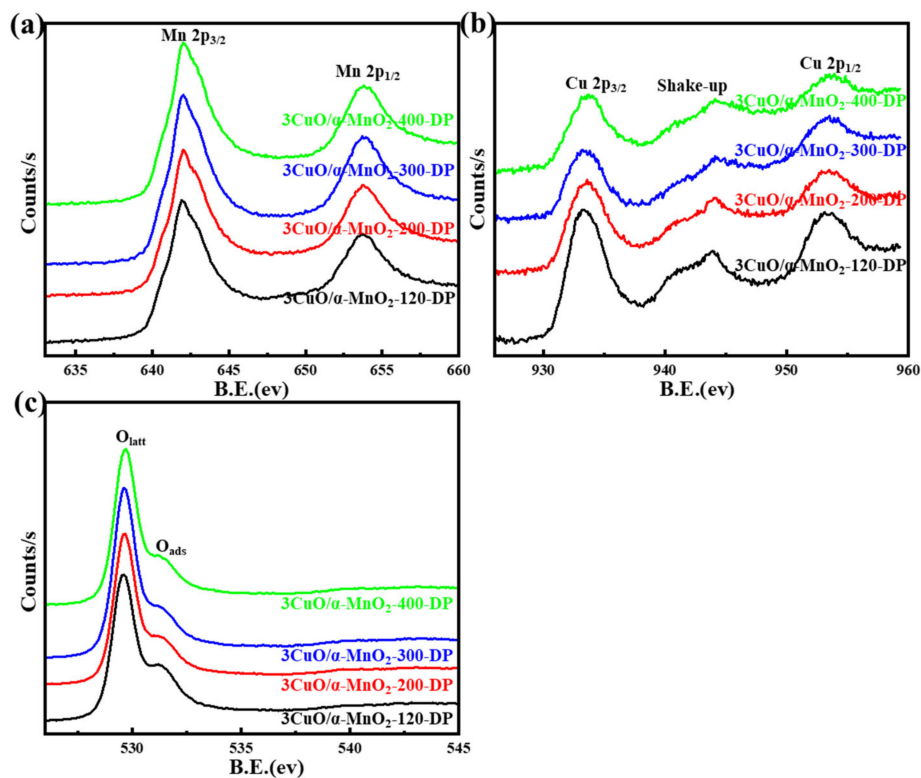


Figure 5. XPS spectra of Mn 2p (a), Cu 2p (b) and O 1s (c) for 3CuO/α-MnO₂-T-IMP catalysts with different calcination temperatures.

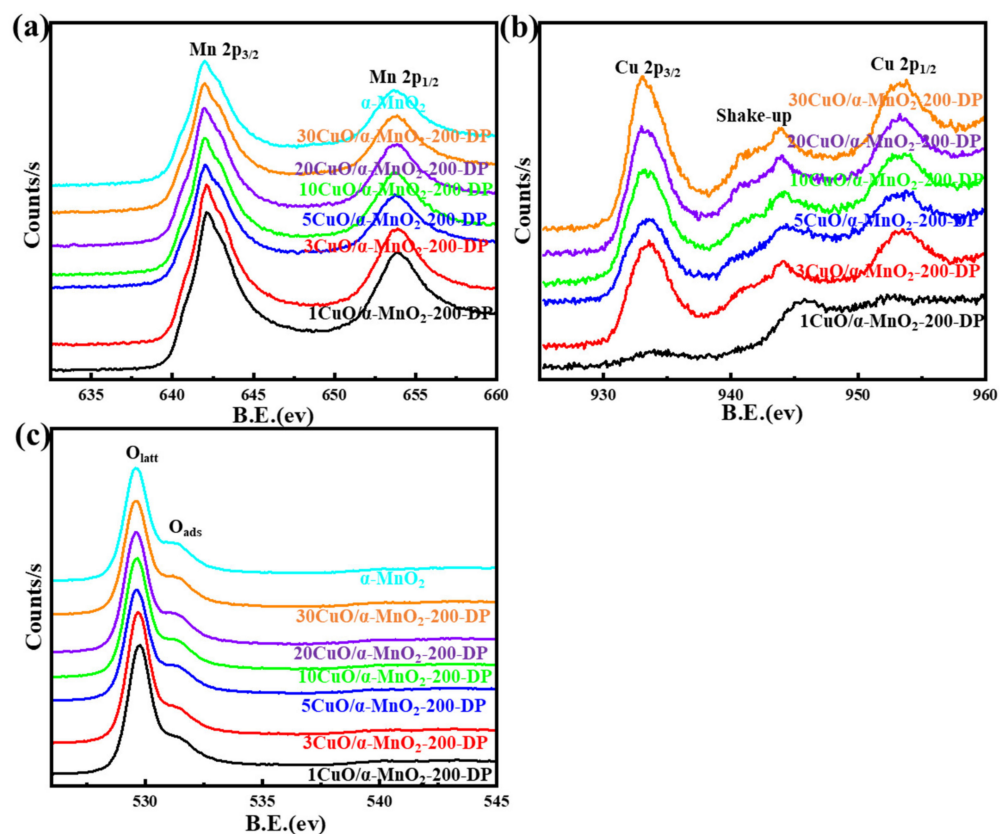


Figure 6. XPS spectra of Mn 2p (a), Cu 2p (b) and O 1s (c) for $x\text{CuO}/\alpha\text{-MnO}_2\text{-200-DP}$ catalysts with different CuO loading.

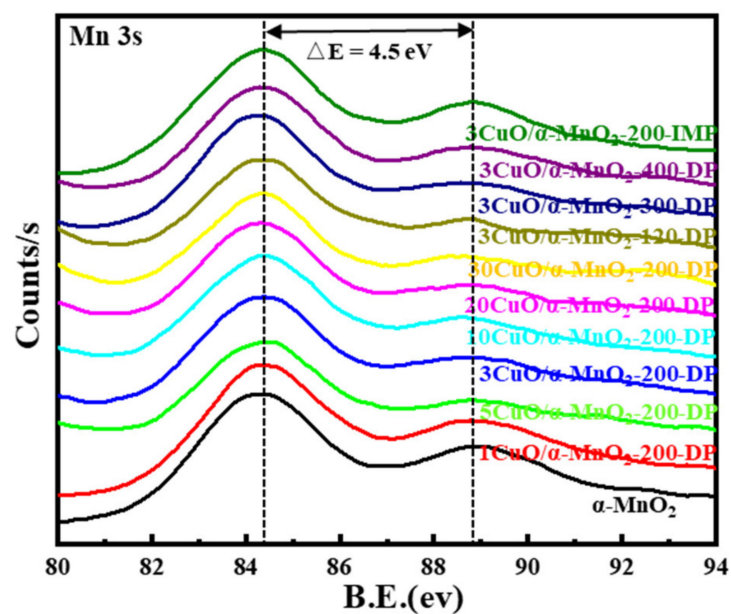


Figure 7. XPS spectra of Mn 3s for catalysts.

Table 1. The surface atomic concentration ratio of Mn, Cu, O of the catalysts based on XPS.

Samples	Mn (%)	Cu (%)	O (%)
α -MnO ₂	21.1	/	46.4
1CuO/ α -MnO ₂ -200-DP	20.8	0.9	45.8
3CuO/ α -MnO ₂ -200-DP	18.1	2.9	51.1
5CuO/ α -MnO ₂ -200-DP	18.0	4.0	44.6
10CuO/ α -MnO ₂ -200-DP	17.8	5.6	43.8
20CuO/ α -MnO ₂ -200-DP	16.5	7.0	39.4
30CuO/ α -MnO ₂ -200-DP	10.0	16.9	40.0
3CuO/ α -MnO ₂ -120-DP	20.4	1.2	45.5
3CuO/ α -MnO ₂ -300-DP	17.7	2.2	44.4
3CuO/ α -MnO ₂ -400-DP	16.9	2.0	41.5
3CuO/ α -MnO ₂ -200-IMP	17.6	1.7	45.9

Table 2. O 1s peak areas of the catalysts based on XPS.

Samples	O 1s Main Peak Area	O 1s Shoulder Peak Area	O 1s Shoulder Peak Area Ratio (%)
α -MnO ₂	129,671.0	32,166.2	19.8
1CuO/ α -MnO ₂ -200-DP	140,985.7	32,068.2	18.5
3CuO/ α -MnO ₂ -200-DP	118,838.6	32,724.9	21.6
5CuO/ α -MnO ₂ -200-DP	138,945.0	32,733.5	19.1
10CuO/ α -MnO ₂ -200-DP	137,120.8	34,822.0	20.3
20CuO/ α -MnO ₂ -200-DP	129,100.5	33,846.1	20.7
30CuO/ α -MnO ₂ -200-DP	129,861.6	32,378.3	20.0
3CuO/ α -MnO ₂ -120-DP	129,997.5	32,051.5	19.8
3CuO/ α -MnO ₂ -300-DP	132,452.1	34,305.7	20.6
3CuO/ α -MnO ₂ -400-DP	134,830.5	33,962.0	20.1
3CuO/ α -MnO ₂ -200-IMP	134,777.2	32,518.3	19.4

Figure 6 shows the XPS spectra of Mn 2p, O 1s and Cu 2p in x CuO/ α -MnO₂-200-DP catalysts with different CuO loadings. As can be seen from Figure 6a, these catalysts had two main peaks at 652.7 eV and 642.0 eV, which were Mn 2p_{1/2} and Mn 2p_{3/2}, respectively. This indicated that Mn existed in the form of Mn⁴⁺ in the x CuO/ α -MnO₂-200-DP catalyst. In order to show the redox characteristics of the prepared catalyst, the surface oxidation state of copper was also studied [39]. As can be seen from Figure 6b, these catalysts had two main peaks at 953.0 eV and 933.0 eV, namely Cu 2p_{1/2} and Cu 2p_{3/2}. It was noteworthy that the peak intensity of the Cu 2p spectrum increased significantly with the increase in copper content, and the corresponding peak fitting results also showed that the proportion of Cu element increased. In order to clarify the properties of various oxygen-containing substances on the x CuO/ α -MnO₂-200-DP catalyst, the XPS spectra of O 1s of all the x CuO/ α -MnO₂-200-DP catalysts are shown in Figure 6c. According to the binding energy of surface elements, the binding energy of the x CuO/ α -MnO₂- T -DP catalyst in Table 3 decreased with the increase in CuO loading. Combined with the data after peak fitting in Table 2, 3CuO/ α -MnO₂-200-DP had the highest acromion area ratio of O 1s. Metal-support interactions between well-dispersed CuO and MnO₂ support produce more surface oxygen and defects. These oxygen and defects predominated when the catalysts exhibited strong CO oxidation properties, and high oxygen vacancy provided a higher catalyst performance for CO catalytic oxidation. In conclusion, different CuO loadings and calcination temperatures together affect the formation of oxygen vacancy on the surface of the catalyst, and further affect the catalytic oxidation performance of CO.

Table 3. Binding energies of surface elements in $x\text{CuO}/\alpha\text{-MnO}_2\text{-}T$ catalysts.

Samples	Cu 2p _{3/2}	O 1s	Mn 2p _{3/2}
$\alpha\text{-MnO}_2$	/	529.8	642.3
1CuO/ $\alpha\text{-MnO}_2\text{-}200\text{-DP}$	933.2	529.7	642.2
3CuO/ $\alpha\text{-MnO}_2\text{-}200\text{-DP}$	933.3	529.7	642.2
5CuO/ $\alpha\text{-MnO}_2\text{-}200\text{-DP}$	933.2	529.6	642.1
10CuO/ $\alpha\text{-MnO}_2\text{-}200\text{-DP}$	933.2	529.6	642.1
20CuO/ $\alpha\text{-MnO}_2\text{-}200\text{-DP}$	933.1	529.6	642.1
30CuO/ $\alpha\text{-MnO}_2\text{-}200\text{-DP}$	933.1	529.6	642.1
3CuO/ $\alpha\text{-MnO}_2\text{-}120\text{-DP}$	933.2	529.6	642.1
3CuO/ $\alpha\text{-MnO}_2\text{-}300\text{-DP}$	933.3	529.6	642.1
3CuO/ $\alpha\text{-MnO}_2\text{-}400\text{-DP}$	933.4	529.7	642.2
3CuO/ $\alpha\text{-MnO}_2\text{-}200\text{-IMP}$	933.3	529.7	642.2

3.1.4. H₂-TPR Analysis

In order to study the interaction between catalyst support and CuO, a H₂-TPR analysis was systematically carried out on the catalysts of commercial MnO₂ and $\alpha\text{-MnO}_2$ nanowire that were loaded with CuO under different CuO loadings, different calcination temperatures and different loading methods. The typical H₂-TPR curve is shown in Figure 7.

Figure 8a shows the H₂-TPR curves of $\alpha\text{-MnO}_2$ nanowire catalyst under different loading modes. With the loading of CuO, the reduction peak of the catalyst moved towards a low temperature, and the reduction in catalyst by precipitation deposition was improved more obviously. This meant that the interaction between CuO and $\alpha\text{-MnO}_2$ nanowire was stronger. Figure 8b shows the H₂-TPR curves of the 3CuO/ $\alpha\text{-MnO}_2\text{-}T\text{-DP}$ nanowire catalysts that were calcined at 120 °C, 200 °C, 300 °C and 400 °C. With the increase in calcination temperature, the relative position between the two reduction peaks of the catalyst basically remained unchanged, and the H₂-TPR curve of the catalysts that were calcined at 200 °C and 300 °C moved to a higher temperature. The increase in CuO composition at this temperature required a higher temperature to completely reduce the catalyst. This indicated that the excellent reduction performance could be reduced by high loading. Figure 8c shows the H₂-TPR curve of $\alpha\text{-MnO}_2$ nanowire with two main peaks, the maximum values of which were concentrated at 372 °C and 613 °C, respectively. The first peak at 372 °C was attributed to the reduction in MnO₂ to Mn₃O₄, while the second peak at 613 °C was attributed to the reduction in Mn₃O₄ to MnO [40]. However, after loading different amounts of CuO, all the $x\text{CuO}/\alpha\text{-MnO}_2\text{-}200\text{-DP}$ catalysts showed a two-stage reduction peak like that of pure $\alpha\text{-MnO}_2$ nanowires, and there was no characteristic reduction peak of CuO species. Meanwhile, the addition of CuO to $\alpha\text{-MnO}_2$ nanowire changed the reduction behavior of $\alpha\text{-MnO}_2$ nanowire. With the increase in CuO loading, the continuous reduction peaks of MnO₂ to Mn₃O₄ and Mn₃O₄ to MnO also shift to lower temperatures. This finding clearly indicated that the CuO had a significant effect on the reduction performance of the $x\text{CuO}/\alpha\text{-MnO}_2\text{-}200\text{-DP}$ catalyst. Figure 8d shows the H₂-TPR curves of commercial MnO₂ and $\alpha\text{-MnO}_2$ nanowire catalysts before and after CuO loading. Unlike $\alpha\text{-MnO}_2$ nanowire, the reduction peak of the commercial MnO₂ catalyst that was loaded with CuO shifts to a high temperature. This meant that the reduction performance of commercial MnO₂ that was loaded with CuO was significantly reduced, indicating that the interaction between CuO and commercial MnO₂ was weak. The structural advantages of $\alpha\text{-MnO}_2$ nanowires and their ability to interact with oxides were shown from the side view.

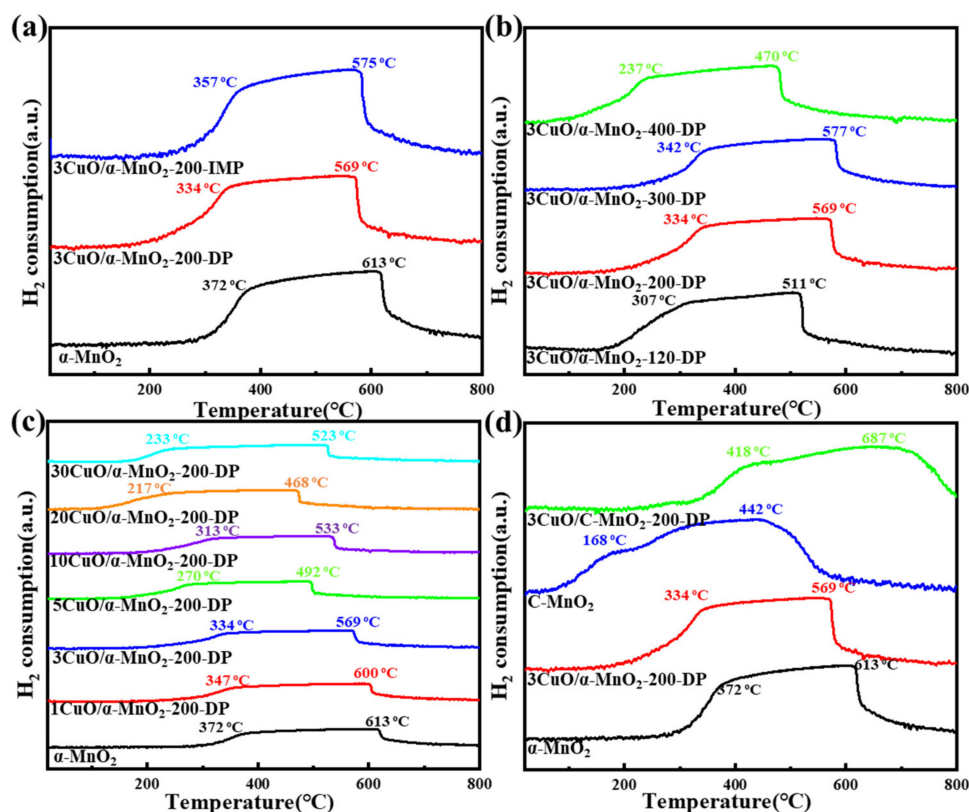


Figure 8. H₂-TPR profiles of (a) α -MnO₂, 3CuO/ α -MnO₂-200-DP and 3CuO/ α -MnO₂-200-IMP catalysts under different loading methods; (b) 3CuO/ α -MnO₂-*T*-DP (*T* = 120, 200, 300, 400) catalysts with different calcination temperatures; (c) *x*CuO/ α -MnO₂-200-DP (*x* = 0, 1, 3, 5, 10, 20, 30) catalysts with different CuO loading; (d) α -MnO₂ nanowire, commercial MnO₂ (C-MnO₂) and corresponding catalysts.

3.2. Catalytic Performance for CO Oxidation

3.2.1. Catalytic Activity

In order to study the influence of the loading mode on the catalytic activity, the catalytic oxidation reaction of 3CuO/ α -MnO₂-200-DP (deposition precipitation method) and the 3CuO/ α -MnO₂-200-IMP (initial impregnation method) catalyst CO was studied. The results are shown in Figure 9a. As can be seen in the figure, the 100% CO conversion temperature of the 3CuO/ α -MnO₂-200-DP catalyst was 80 °C. The catalytic activity of the 3CuO/ α -MnO₂-200-IMP catalyst was much lower than that of the 3CuO/ α -MnO₂-200-DP catalyst, and the complete transformation of CO can be realized until 170 °C. This shows that the sedimentation method has obvious advantages over the traditional initial impregnation method.

To study the influence of calcination temperature on the catalytic activity of the 3CuO/ α -MnO₂-*T*-DP catalyst, the CO catalytic oxidation reaction was studied at calcination temperatures of 200 °C, 300 °C and 400 °C, and catalyst samples dried only at 120 °C without calcination, as shown in Figure 9b. As can be seen from the figure, the catalytic activity of 3CuO/ α -MnO₂-*T*-DP catalyst decreases as the calcination temperature increases from 200 °C to 400 °C. The catalytic activity of catalysts that have been calcined at 120 °C, was lower than that of the catalyst samples that have been calcined at 200 °C to 400 °C. This may be because Cu(NO₃)₂·3H₂O did not decompose completely due to the low temperature of catalyst samples that were calcined above 200 °C during the loading process. The calcination temperature of the catalysts had great influence on the dispersion, structure and metal–surface interaction strength of the catalysts. It can be seen from the XRD pattern that the CuO diffraction peak intensity of 3CuO/ α -MnO₂-*T*-DP catalyst was different to some extent. The CuO diffraction peak of 3CuO/ α -MnO₂-300-DP was the

strongest, indicating that the CuO species were poorly dispersed. Therefore, the different catalytic activity of the $3\text{CuO}/\alpha\text{-MnO}_2\text{-}T\text{-DP}$ catalyst at different calcination temperatures may be related to the dispersion of CuO active sites. In addition, the difference in catalytic activity of $3\text{CuO}/\alpha\text{-MnO}_2\text{-}T\text{-DP}$ catalysts at different calcination temperatures may also be caused by the thermal shrinkage of the catalyst skeleton and the agglomeration of CuO species.

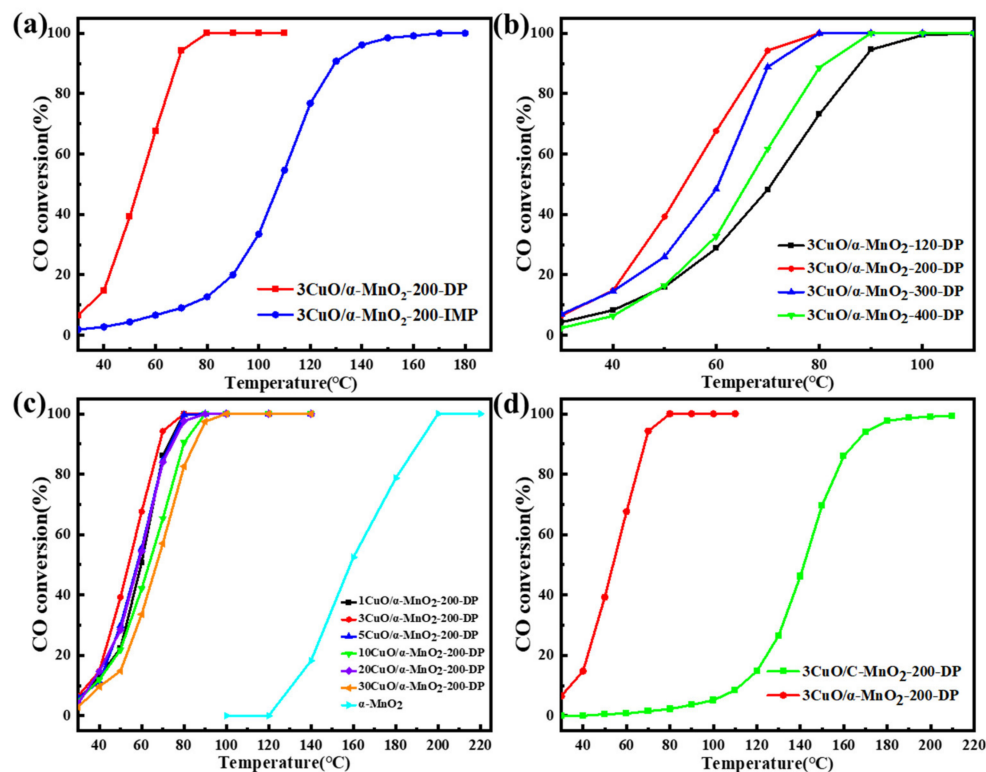


Figure 9. (a) $3\text{CuO}/\alpha\text{-MnO}_2\text{-}200\text{-DP}$ and $3\text{CuO}/\alpha\text{-MnO}_2\text{-}200\text{-IMP}$ catalysts under different loading modes; (b) $3\text{CuO}/\alpha\text{-MnO}_2\text{-}T\text{-DP}$ ($T = 120, 200, 300, 400$) catalysts; (c) $x\text{CuO}/\alpha\text{-MnO}_2\text{-}200$ ($x = 0, 1, 3, 5, 10, 20, 30$) catalyst; and (d) CO conversion of pure $\alpha\text{-MnO}_2$ nanowires and commercial MnO_2 catalysts supported by CuO by precipitation deposition at different reaction temperatures.

Secondly, the catalytic activity of CO oxidation on the $x\text{CuO}/\alpha\text{-MnO}_2\text{-}200\text{-DP}$ catalyst with CuO loading was evaluated in detail, as shown in Figure 9c. As can be seen from the figure, pure $\alpha\text{-MnO}_2$ nanowire catalyst started to activate at 120°C . With the increase in reaction temperature, CO conversion gradually increased until reaching 100% at about 200°C . Compared with pure $\alpha\text{-MnO}_2$ nanowire carrier, the $x\text{CuO}/\alpha\text{-MnO}_2\text{-}200\text{-DP}$ catalyst had higher catalytic activity, especially in the $30\text{--}100^\circ\text{C}$ region. These results indicated that CuO species were the main active center of CO oxidation and the main cause of CO oxidation at a low temperature. To show the difference more clearly in the catalytic activity of the $x\text{CuO}/\alpha\text{-MnO}_2\text{-}200\text{-DP}$ catalysts with different CuO loads, the CO conversion of the $x\text{CuO}/\alpha\text{-MnO}_2\text{-}200\text{-DP}$ catalysts was analyzed at 60°C , as shown in Figure 10. When the CuO load increased from 0 wt% to 3 wt%, the catalytic activity of the $x\text{CuO}/\alpha\text{-MnO}_2\text{-}200\text{-DP}$ catalyst was significantly enhanced at a low temperature. The $3\text{CuO}/\alpha\text{-MnO}_2\text{-}200\text{-DP}$ catalyst showed the highest catalytic activity among all the catalysts, which showed a significant advantage compared with previous studies. However, a further increase in CuO from 3 wt% to 30 wt% lead to a decrease in catalytic activity. The possible reason was that the one-dimensional structure of $\alpha\text{-MnO}_2$ nanowires, especially the aspect ratio of the catalyst, decreases significantly with the increase in CuO load, resulting in a poor dispersion of CuO on the surface of the supports.

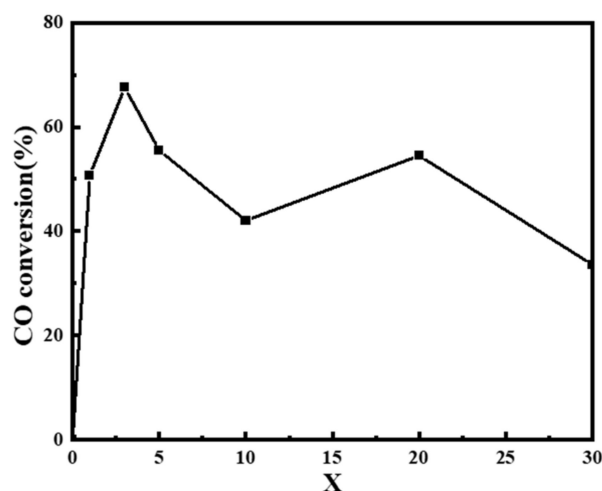


Figure 10. CO conversion and conversion of $x\text{CuO}/\alpha\text{-MnO}_2\text{-200-DP}$ ($x = 0, 1, 3, 5, 10, 20, 30$) catalysts with different CuO loading at $60\text{ }^\circ\text{C}$.

Meanwhile, in order to study the influence of the nanowire structure and redox performance of the catalyst support on the catalytic activity, commercial MnO_2 was used as the contrast carrier for the CO catalytic oxidation reaction and the same loading method was used to prepare the contrast catalyst. Figure 9d shows the catalytic activity of comparative catalysts. In the figure, the 100% CO conversion temperature of the $3\text{CuO}/\alpha\text{-MnO}_2\text{-200-DP}$ catalyst was $80\text{ }^\circ\text{C}$, while the CO conversion of the $3\text{CuO}/\text{C-MnO}_2\text{-200-DP}$ catalyst was close to 100% only when the temperature was above $200\text{ }^\circ\text{C}$. The catalytic activity of the $3\text{CuO}/\text{C-MnO}_2\text{-200-DP}$ catalyst was like the $\alpha\text{-MnO}_2$ nanowire support without the CuO load. The advantages of the structure and properties of $\alpha\text{-MnO}_2$ nanowire support were illustrated.

3.2.2. Long-Term Stability Test

A long-term stability test was carried out to evaluate the catalytic stability of the prepared CuO-based catalyst under the specific reaction conditions ($\text{CO}/\text{O}_2/\text{N}_2 = 1/20/79$, $\text{GHSV} = 12,000\text{ mL}\cdot\text{g}^{-1}\cdot\text{h}^{-1}$, $80\text{ }^\circ\text{C}$, 1 atm). The CO oxidation stability of these catalysts was tested for 12 h, and $3\text{CuO}/\alpha\text{-MnO}_2\text{-200-DP}$ was selected as the representative catalyst. As can be seen from Figure 11, the $3\text{CuO}/\alpha\text{-MnO}_2\text{-200-DP}$ catalyst showed excellent stability during the entire 12 h stability test, with the activity remaining at 100% and no significant deactivation. These results indicate that the $3\text{CuO}/\alpha\text{-MnO}_2\text{-200-DP}$ catalyst not only had high temperature activity, but also had good stability.

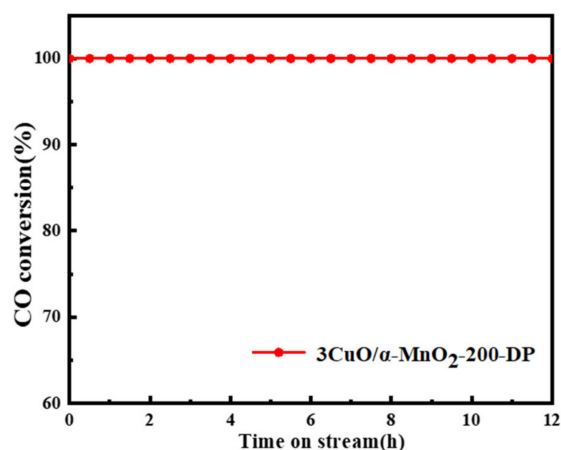


Figure 11. Stability of $3\text{CuO}/\alpha\text{-MnO}_2\text{-200-DP}$ catalyst at $80\text{ }^\circ\text{C}$ for 12 h.

4. Conclusions

In summary, a series of CuO/ α -MnO₂ nanowire catalysts with different CuO loadings, different calcination temperatures and different loading modes were synthesized as the supports of a CO catalytic oxidation catalyst. The slenderness ratio of the CuO/ α -MnO₂ nanowire catalyst decreases with the increase in loading capacity. The results showed that when CuO loading was 3 wt%, calcination temperature was 200 °C and the catalyst that was supported by the deposition precipitation method had the highest catalytic activity. Compared with the commercial MnO₂ catalyst, the synthetic α -MnO₂ nanowire catalyst has better redox performance and better low-temperature catalytic activity due to the particularity of the microstructure. Compared with commercial MnO₂, it was a better catalyst support for CO catalytic oxidation. The CuO particles that were calcined at 200 °C by the precipitation deposition method showed better dispersion on the surface of a α -MnO₂ nanowire support, which proved that the precipitation deposition method was superior to the traditional initial impregnation method. In addition, CuO as the active center of CO oxidation formed a strong intermetallic synergistic effect on the surface of the α -MnO₂ nanowire support, which further enhanced the CO oxidation activity of the α -MnO₂ nanowire support at a low temperature. Because of these advantages, α -MnO₂ nanowire is considered as a promising support for the CO oxidation of CuO-based catalysts, and has stronger catalytic activity, especially at low temperatures.

Author Contributions: Conceptualization, M.C. and Y.C.; formal analysis, H.S. and P.G.; investigation, H.S. and Y.C.; resources, M.C.; data curation, Y.S.; writing—original draft preparation, Y.C.; writing—review and editing, L.X.; funding acquisition, M.C. All authors have read and agreed to the published version of the manuscript.

Funding: This research was funded by the National Natural Science Foundation of China (grant number 21976094, 22176100, 21871144) and the Postgraduate Research & Practice Innovation Program of Jiangsu Province in 2022 (KYCX22_1216).

Data Availability Statement: The data supporting the findings of this study are available by reasonable request to chenmd@nuist.edu.cn.

Conflicts of Interest: The authors declare no conflict of interest.

References

1. Namasivayam, A.M.; Korakianitis, T.; Crookes, R.J.; Bob-Manuel, K.D.H.; Olsen, J. Biodiesel, Emulsified Biodiesel and Dimethyl Ether as Pilot Fuels for Natural Gas Fuelled Engines. *Appl. Energy* **2010**, *87*, 769–778. [[CrossRef](#)]
2. Neidell, M.J. Air Pollution, Health, and Socio-Economic Status: The Effect of Outdoor Air Quality on Childhood Asthma. *J. Health Econ.* **2004**, *23*, 1209–1236. [[CrossRef](#)] [[PubMed](#)]
3. Prado, O.J.; Veiga, M.C.; Kennes, C. Removal of Formaldehyde, Methanol, Dimethylether and Carbon Monoxide from Waste Gases of Synthetic Resin-Producing Industries. *Chemosphere* **2008**, *70*, 1357–1365. [[CrossRef](#)] [[PubMed](#)]
4. Lee, J.G.; An, K. Catalytic Co Oxidation on Nanocatalysts. *Top. Catal.* **2018**, *61*, 986–1001. [[CrossRef](#)]
5. Wang, L.; Wang, L.; Zhang, J.; Wang, H.; Xiao, F.-S. Enhancement of the Activity and Durability in CO Oxidation over Silica-Supported Au Nanoparticle Catalyst Via Ceox Modification. *Chin. J. Catal.* **2018**, *39*, 1608–1614. [[CrossRef](#)]
6. Zheng, B.; Wu, S.; Yang, X.; Jia, M.; Zhang, W.; Liu, G. Room Temperature Co Oxidation over Pt/MgFe₂O₄: A Stable Inverse Spinel Oxide Support for Preparing Highly Efficient Pt Catalyst. *ACS Appl. Mater. Interfaces* **2016**, *8*, 26683–26689. [[CrossRef](#)]
7. Camposeco, R.; Hinojosa-Reyes, M.; Castillo, S.; Nava, N.; Zanella, R. Synthesis and Characterization of Highly Dispersed Bimetallic Au-Rh Nanoparticles Supported on Titanate Nanotubes for CO Oxidation Reaction at Low Temperature. *Environ. Sci. Pollut. Res.* **2021**, *28*, 10734–10748. [[CrossRef](#)]
8. Zhang, X.; Li, G.; Tian, R.; Feng, W.; Wen, L. Monolithic Porous CuO/CeO₂ Nanorod Composites Prepared by Dealloying for CO Catalytic Oxidation. *J. Alloys Compd.* **2020**, *826*, 154149. [[CrossRef](#)]
9. Kong, F.; Zhang, H.; Chai, H.; Liu, B.; Cao, Y. Insight into the Crystal Structures and Surface Property of Manganese Oxide on Co Catalytic Oxidation Performance. *Inorg. Chem.* **2021**, *60*, 5812–5820. [[CrossRef](#)]
10. Murthy, P.R.; Munsif, S.; Zhang, J.-C.; Li, W.-Z. Influence of CeO₂ and ZrO₂ on the Thermal Stability and Catalytic Activity of Sba-15-Supported Pd Catalysts for Co Oxidation. *Ind. Eng. Chem. Res.* **2021**, *60*, 14424–14433. [[CrossRef](#)]
11. Sun, L.; Zhan, W.; Li, Y.-A.; Wang, F.; Zhang, X.; Han, X. Understanding the Facet-Dependent Catalytic Performance of Hematite Microcrystals in a Co Oxidation Reaction. *Inorg. Chem. Front.* **2018**, *5*, 2332–2339. [[CrossRef](#)]

12. Baidya, T.; Murayama, T.; Nellaiappan, S.; Katiyar, N.K.; Bera, P.; Safonova, O.; Lin, M.; Priolkar, K.R.; Kundu, S.; Rao, B.S.; et al. Ultra-Low-Temperature Co Oxidation Activity of Octahedral Site Cobalt Species in CO_3O_4 Based Catalysts: Unravelling the Origin of the Unique Catalytic Property. *J. Phys. Chem. C* **2019**, *123*, 19557–19571. [[CrossRef](#)]
13. Lou, Y.; Wang, L.; Zhao, Z.; Zhang, Y.; Zhang, Z.; Lu, G.; Guo, Y.; Guo, Y. Low-Temperature CO Oxidation over CO_3O_4 -Based Catalysts: Significant Promoting Effect of Bi_2O_3 on CO_3O_4 Catalyst. *Appl. Catal. B Environ.* **2014**, *146*, 43–49. [[CrossRef](#)]
14. Cui, Y.; Xu, L.; Chen, M.; Lv, C.; Lian, X.; Wu, C.-E.; Yang, B.; Miao, Z.; Wang, F.; Hu, X. Co Oxidation over Metal Oxide (La_2O_3 , Fe_2O_3 , PrO_2 , Sm_2O_3 , and MnO_2) Doped CuO-Based Catalysts Supported on Mesoporous $\text{Ce}_{0.8}\text{Zr}_{0.2}\text{O}_2$ with Intensified Low-Temperature Activity. *Catalysts* **2019**, *9*, 724. [[CrossRef](#)]
15. Ren, Y.; Ma, Z.; Qian, L.; Dai, S.; He, H.; Bruce, P.G. Ordered Crystalline Mesoporous Oxides as Catalysts for Co Oxidation. *Catal. Lett.* **2009**, *131*, 146–154. [[CrossRef](#)]
16. Song, H.; Xu, L.; Chen, M.; Cui, Y.; Wu, C.-E.; Qiu, J.; Xu, L.; Cheng, G.; Hu, X. Recent Progresses in the Synthesis of MnO_2 Nanowire and Its Application in Environmental Catalysis. *RSC Adv.* **2021**, *11*, 35494–35513. [[CrossRef](#)]
17. Zhao, G.-Y.; Li, H.-L. Electrochemical Oxidation of Methanol on Pt Nanoparticles Compositing MnO_2 Nanowire Arrayed Electrode. *Appl. Surf. Sci.* **2008**, *254*, 3232–3235. [[CrossRef](#)]
18. Ren, Y.; Ma, Z.; Dai, S. Nanosize Control on Porous Beta- MnO_2 and Their Catalytic Activity in Co Oxidation and N_2O Decomposition. *Materials* **2014**, *7*, 3547–3556. [[CrossRef](#)]
19. Jampaiah, D.; Velisoju, V.K.; Venkataswamy, P.; Coyle, V.E.; Nafady, A.; Reddy, B.M.; Bhargava, S.K. Nanowire Morphology of Mono- and Bidoped Alpha- MnO_2 Catalysts for Remarkable Enhancement in Soot Oxidation. *ACS Appl. Mater. Interfaces* **2017**, *9*, 32652–32666. [[CrossRef](#)]
20. Du, H.; Wang, Y.; Arandiyani, H.; Younis, A.; Scott, J.; Qu, B.; Wan, T.; Lin, X.; Chen, J.; Chu, D. Design and Synthesis of CeO_2 Nanowire/ MnO_2 Nanosheet Heterogeneous Structure for Enhanced Catalytic Properties. *Mater. Today Commun.* **2017**, *11*, 103–111. [[CrossRef](#)]
21. Saputra, E.; Muhammad, S.; Sun, H.; Patel, A.; Shukla, P.; Zhu, Z.H.; Wang, S. Alpha- MnO_2 Activation of Peroxymonosulfate for Catalytic Phenol Degradation in Aqueous Solutions. *Catal. Commun.* **2012**, *26*, 144–148. [[CrossRef](#)]
22. Liang, S.; Bulgan, F.T.G.; Zong, R.; Zhu, Y. Effect of Phase Structure of MnO_2 Nanorod Catalyst on the Activity for Co Oxidation. *J. Phys. Chem. C* **2008**, *112*, 5307–5315. [[CrossRef](#)]
23. Zhang, Y.; Deng, S.; Luo, M.; Pan, G.; Zeng, Y.; Lu, X.; Ai, C.; Liu, Q.; Xiong, Q.; Wang, X.; et al. Defect Promoted Capacity and Durability of N- MnO_{2-x} Branch Arrays Via Low-Temperature NH_3 Treatment for Advanced Aqueous Zinc Ion Batteries. *Small* **2019**, *15*, 1905452. [[CrossRef](#)]
24. Selvakumar, K.; Duraisamy, V.; Venkateshwaran, S.; Arumugam, N.; Almansour, A.I.; Wang, Y.; Liu, T.X.; Kumar, S.M.S. Development of Alpha- MnO_2 Nanowire with Ni- and (Ni, Co)-Cation Doping as an Efficient Bifunctional Oxygen Evolution and Oxygen Reduction Reaction Catalyst. *ChemElectroChem* **2022**, *9*, e202101303. [[CrossRef](#)]
25. Wang, J.; Luo, H.; Liu, P. Highly Dispersed Gold Nanoparticles on Metal-Doped Alpha- MnO_2 Catalysts for Aerobic Selective Oxidation of Ethanol. *Catal. Commun.* **2020**, *142*, 106030. [[CrossRef](#)]
26. Li, X.; Cheng, H.; Liang, G.; He, L.; Lin, W.; Yu, Y.; Zhao, F. Effect of Phosphine Doping and the Surface Metal State of Ni on the Catalytic Performance of Ni/ Al_2O_3 Catalyst. *Catalysts* **2015**, *5*, 759–773. [[CrossRef](#)]
27. Hashem, A.M.; Abuzeid, H.M.; Narayanan, N.; Ehrenberg, H.; Julien, C.M. Synthesis, Structure, Magnetic, Electrical and Electrochemical Properties of Al, Cu and Mg Doped MnO_2 . *Mater. Chem. Phys.* **2011**, *130*, 33–38. [[CrossRef](#)]
28. Gao, J.; Jia, C.; Zhang, L.; Wang, H.; Yang, Y.; Hung, S.-F.; Hsu, Y.-Y.; Liu, B. Tuning Chemical Bonding of MnO_2 through Transition-Metal Doping for Enhanced CO Oxidation. *J. Catal.* **2016**, *341*, 82–90. [[CrossRef](#)]
29. Zhang, Z.; Tian, Y.; Zhao, W.; Wu, P.; Zhang, J.; Zheng, L.; Ding, T.; Li, X. Hydroxyl Promoted Preferential and Total Oxidation of Co over Epsilon- MnO_2 Catalyst. *Catal. Today* **2020**, *355*, 214–221. [[CrossRef](#)]
30. Xu, R.; Wang, X.; Wang, D.S.; Zhou, K.B.; Li, Y.D. Surface Structure Effects in Nanocrystal MnO_2 and Ag/MnO_2 Catalytic Oxidation of CO. *J. Catal.* **2006**, *237*, 426–430. [[CrossRef](#)]
31. Tuan Sang, T.; Tripathi, K.M.; Kim, B.N.; You, I.-K.; Park, B.J.; Han, Y.H.; Kim, T. Three-Dimensionally Assembled Graphene/Alpha- MnO_2 Nanowire Hybrid Hydrogels for High Performance Supercapacitors. *Mater. Res. Bull.* **2017**, *96*, 395–404.
32. Qian, K.; Qian, Z.; Hua, Q.; Jiang, Z.; Huang, W. Structure-Activity Relationship of CuO/MnO_2 Catalysts in CO Oxidation. *Appl. Surf. Sci.* **2013**, *273*, 357–363. [[CrossRef](#)]
33. Kumar, J.P.; Ramachatyulu, P.V.R.K.; Prasad, G.K.; Singh, B. Montmorillonites Supported with Metal Oxide Nanoparticles for Decontamination of Sulfur Mustard. *Appl. Clay Sci.* **2015**, *116*, 263–272. [[CrossRef](#)]
34. Papadas, I.T.; Ioakeimidis, A.; Vamvasakis, I.; Eleftheriou, P.; Armatas, G.S.; Choulis, S.A. All-Inorganic P-N Heterojunction Solar Cells by Solution Combustion Synthesis Using N-Type FeMnO_3 Perovskite Photoactive Layer. *Front. Chem.* **2021**, *9*, 803. [[CrossRef](#)]
35. Tafur, J.P.; Abad, J.; Roman, E.; Fernandez Romero, A.J. Charge Storage Mechanism of MnO_2 Cathodes in Zn/ MnO_2 Batteries Using Ionic Liquid-Based Gel Polymer Electrolytes. *Electrochem. Commun.* **2015**, *60*, 190–194. [[CrossRef](#)]
36. Kawai, J.; Maeda, K.; Nakajima, K.; Gohshi, Y. Relation between Copper L X-ray Fluorescence and 2p X-ray Photoelectron Spectroscopies. *Phys. Rev. B* **1993**, *48*, 8560–8566. [[CrossRef](#)]
37. Du, J.; Xiao, G.; Xi, Y.; Zhu, X.; Su, F.; Kim, S.H. Periodate Activation with Manganese Oxides for Sulfanilamide Degradation. *Water Res.* **2020**, *169*, 115278. [[CrossRef](#)]

38. McKinney P V, Reduction of palladium oxide by carbon monoxide. *J. Am. Chem. Soc.* **1932**, *54*, 4498–4504. [[CrossRef](#)]
39. Freitas, I.C.; Damyanova, S.; Oliveira, D.C.; Marques, C.M.P.; Bueno, J.M.C. Effect of Cu Content on the Surface and Catalytic Properties of Cu/ZrO₂ Catalyst for Ethanol Dehydrogenation. *J. Mol. Catal. A Chem.* **2014**, *381*, 26–37. [[CrossRef](#)]
40. Sun, M.; Lan, B.; Lin, T.; Cheng, G.; Ye, F.; Yu, L.; Cheng, X.; Zheng, X. Controlled Synthesis of Nanostructured Manganese Oxide: Crystalline Evolution and Catalytic Activities. *CrystEngComm* **2013**, *15*, 7010–7018. [[CrossRef](#)]